**Proceedings of the ASME 2021
International Mechanical Engineering Congress and Exposition
IMECE2021
November 1-5, 2021, Virtual, Online**

# IMECE2021-72854



# A COMPUTATIONAL ANALYSIS OF BUBBLE-STRUCTURE INTERACTION IN NEAR-FIELD UNDERWATER EXPLOSION

**Wentao Ma, Timothy Ozenkoski, Kevin Wang***
Department of Aerospace and Ocean Engineering
Virginia Polytechnic Institute and State University
Blacksburg, Virginia 24061

## ABSTRACT

*Underwater explosion poses a significant threat to the structural integrity of ocean vehicles and platforms. Accurate prediction of the dynamic loads from an explosion and the resulting structural response is crucial to ensuring safety without overconservative design. When the distance between the explosive charge and the structure is relatively small (i.e., near-field explosion), the dynamics of the gaseous explosion product, i.e., the "bubble", comes into play, rendering a multiphysics problem that features the interaction of the bubble, the surrounding liquid water, and the solid structure. The problem is highly nonlinear, as it involves shock waves, large deformation, yielding, contact, and possibly fracture. This paper investigates the two-way interaction between the cyclic expansion and collapse of an explosion bubble and the deformation of a thin-walled elastoplastic cylindrical shell in its vicinity. Intuitively, when a shock wave impinges on a thin cylindrical shell, the shell would collapse in the direction of shock propagation. However, some recent laboratory experiments have shown that under certain conditions the shell collapsed in a counter-intuitive mode in which the direction of collapse is perpendicular to that of shock propagation. In other words, the nearest point on the structural surface moved towards the explosion charge, despite being impacted by a compressive shock. This paper focuses on replicating this phenomenon through numerical simulation and elucidating the underlying mechanisms. A recently developed computational framework ("FIVER") coupling a nonlinear finite element structural dynamics solver and a finite volume compressible fluid dynamics solver is used to complete this study. The solver utilizes an embedded boundary method to track the wetted surface of the structure (i.e. the fluid-structure interface), which is capable of handling large structural deformation and topological changes (e.g., fracture). The solver also adopts the level set method for tracking the bubble surface (i.e. the liquid-gas interface). The fluid-structure and liquid-gas interface conditions are enforced by constructing and solving one-dimensional multi-material Riemann problems, which naturally accommodates the propagation of shock waves across the interfaces. In this paper, mesh refinement study is made to examine the sensitivity of the results to various meshing parameters. The results show that the intermediate level of refinement is appropriate in terms of both the accuracy and the computation costs. Next, the deformation history of both the bubble and the structure are presented and analyzed to provide a detailed view of the counter-intuitive collapse mode mentioned above. We show that timewise, the structural collapse spans multiple cycles of bubble oscillation. Additional details about the time-histories of fluid pressure, structure displacement, and bubble size are presented to elucidate this dynamic bubble-structure interaction and the resulting structural failure.*

Keywords: fluid-structure interaction, underwater explosion, bubble dynamics, collapse, simulation

## 1. INTRODUCTION

Submerged structures and vehicles are susceptible to damage and collapse induced by both near-field and far-field underwater explosions. These explosions typically consist of two primary parts: the bubble located at the origin of the explosion, and the shock wave that is formed from the explosion. In free field, the shock wave profile can be readily described using a combination of experimentally determined data and an exponentially decaying function, such as Cole's Model [1]. The fluid-structure interaction induced by both the shock wave and the bubble dynamics, however, is more complex and generally requires a coupled simulation or laboratory experiment to fully and accurately describe the phenomena. When dealing with near-

* Corresponding author. E-mail address: kevinwgy@vt.edu

 

field and far-field explosions, the loading effects can generally be broken down into three different conditions.

1. The explosion is a far-field explosion and the only loading the structure undergoes is the planar shockwave from the explosion (e.g., [2-4]).
2. The explosion is an extreme near-field explosion in which the bubble is close enough to the structure that it pulls towards it and merges on the structure's wetted surface (e.g., [5,6]).
3. The explosion is a near-field explosion in which the bubble is sufficiently far away from the structure that it does not merge with the structure, but the structure undergoes loading from the pulsation of the bubble (e.g., [7-9]).

In condition 1, the bubble created is far enough away from the structure that the two do not interact, and the effects of bubble pulsation can be ignored. As a result, the primary effect from the explosion that should be considered is a shock wave that can often be assumed to be planar. The dynamic response and failure of structures under shock waves produced by far-field explosions have been studied extensively in the past. For example, various studies (e.g., [2-4]) have shown how explosions can cause damage or collapse on various structures, including ship hulls, underwater pipelines, and submarines. These large pressure waves can cause large plastic deformations in a structure and can easily cause severe damaging. Bartolini *et al.* discusses how varying the distance between the explosion origin and structure can impact whether a thin cylindrical shell would collapse under a specific loading condition [10]. Of the three conditions mentioned above, this is probably the simplest to model.

In the case of a near-field explosion, conditions 2 and 3 are both possible. In condition 2, if the bubble is adjacent to the structure, the bubble will pull towards it and merge with the structure's surface. This can have catastrophically damaging effects as when the bubble expands, it may have a pressure much lower than the hydrostatic pressure of the surrounding fluid. When the bubble is initially formed, the pressure inside is much higher than the hydrostatic pressure of the medium surrounding it. As the bubble expands, the bubble pressure can decrease below the hydrostatic pressure of the fluid, creating a region on the surface of the structure where the pressure distribution varies significantly. For example, Brett and Yiannakopolous discusses this phenomenon and highlights how this interaction is largely more damaging than the pulsation of the bubble and even the initial contact of the shock wave [11].

The third condition is one where the bubble is close enough to the structure that the pulsation can have an influence on its deformation but is sufficiently far away so that the bubble does not merge with the structure. This condition is less severe than the other near-field condition but is still potentially more damaging than the far-field alternative. Due to the close proximity of the explosion to the structure, the shock wave from a weaker explosion can be just as impactful as a larger explosion much farther away. Additionally, if the structure is deformed from the initial shock wave, then the following pulsations can act to further deform and damage it. These pulsations are typically lower in magnitude than the initial load but can act to increase the damage on an already damaged structure. Various numerical studies have been used to show this phenomena, and multiple experiments have been performed in [12,13].

In an underwater explosion, it is shown that the bubble formed does not purely expand and then disperse. Due to the explosion, the bubble initially has a small radius and an internal pressure much higher than that of the surrounding fluid. As the radius of the bubble increases, the internal pressure of the bubble decreases until the hydrostatic pressure of the surrounding fluid is then higher than the pressure of the bubble, which in turn causes for the bubble's radius to decrease until the internal pressure is once again higher than that of the surrounding fluid. Depending on the loading conditions and boundary conditions, the bubble will continue this oscillation in size until it initially disperses. For every oscillation of the bubble, a pressure pulse is propagated through the surrounding medium and significant energy is taken out of the system. After enough energy has been taken out, the bubble will finally collapse, and the pulsation will stop.

Although the bubble is initially shaped spherically, throughout its pulsation multiple forces interact with it to cause shape deformation [14]. As the bubble pulsates, a jet stream may form around it, pushing into the center of the bubble. If this stream is powerful enough, it can perturb through the bubble and cause it to break into two separate bubbles. Other factors, such as the materials used to cause the explosion, the shape of the initial charge, and the style of detonation can also influence the initial shape of the bubble and its collapse. Zhang *et al.* refers to this as "*the memory effect*" as the bubbles "remembers" the conditions it was initially created under and is influenced by those conditions as well [14].

In this paper, we investigate the two-way interaction between the dynamics of an explosion bubble and the deformation and collapse of a thin-walled elastoplastic cylindrical shell, in the context of near-field explosion in which the bubble is close to the structural surface but does not merge with it. Although a thin-walled cylindrical shell is a broad term, it has a number of practical applications, and results from its collapse can be related to structural applications on both submarines and underwater pipelines. In both of these cases, the collapse condition of the structure is dependent on a number of variables, including material properties, ovality, eccentricity, the length/thickness ratio, and the diameter/thickness ratio [15].

While most research on submarines is classified, several applicable papers have been published regarding the collapse of cylindrical tubes under hydrostatic loading, shock-induced loading, and the combined loading of both these conditions. Ikeda presented a study that discussed how the length/diameter ratio influenced the mode of collapse of a cylindrical shell and found that models with a larger length/diameter ratio collapsed in mode 2, whereas models with a smaller ratio collapsed in a higher mode [16]. Kyriakides *et al.* also performed multiple investigations on how imperfections and characteristics of the geometry of a cylindrical shell would influence collapse, including studies on denting [17], localization of collapse on finite-length shells [18], and the collapse of long cylindrical shells under the combined loads of external hydrostatic pressure and bending [19].

While the dimensions of a manufactured cylindrical shell have been shown to impact the collapse pressure of the structure, imperfections caused by manufacturing processes can also have a significant impact as well. During manufacturing, these shells (i.e., pipelines) commonly undergo a cold-form manufacturing process that typically leave a pipeline with an ovality < 1.0% and rarely exceeding 2% [20-22]. Even an ovality of 1% can have a significant impact on the critical pressure of a cylindrical shell, potentially reducing the collapse pressure of a thick-walled pipeline by over 25% [23]. An ovality of 10% would have even more drastic influence on the critical pressure of a cylinder, reducing it to 50% that of a cylindrical shell that had no ovality [16].

The dynamics of collapse for a bubble work in tandem with the geometric properties, material properties, and imperfections of the cylindrical shell to influence collapse. In the case of this numerical experiment, the complex behaviors of bubble pulsation are paired with hydrostatic pressure, physical properties, and the imperfections of ovality to create an atypical collapse behavior where the structure is pulled towards the bubble instead of collapsing in the direction of the initial shock wave. This complex study is performed using a three-dimensional CFD (computational fluid dynamics) – CSD (computational structural dynamics) coupled model, in which information such as a fluid velocity field, structural nodal displacement, fluid pressure, and structural strain can all be determined. This includes a Navier-Stokes CFD solver, which is capable of tracking fluid-fluid interfaces between the bubble and the surrounding water. A second-order embedded boundary method capable of handling large deformations is incorporated as well.

This numerical experiment details the collapse of a thin-walled aluminum cylindrical shell under the combined loading from a near-field explosion and from hydrostatic pressure. It holds geometric imperfections, such as initial ovality, and there is no eccentricity on the shell. This solver produces a time-history of collapse, which is analyzed, and the phenomena inducing atypical collapse behavior are discussed.

## 2. PHYSICAL MODEL AND NUMERICAL METHODS

*Figure 1* details the model used to demonstrate the collapse of the thin cylindrical shell. The cylindrical shell has a thickness of 0.711 mm and an outer diameter of 38.911 mm. Numbers 1-4 denote multiple sensors. Sensor 1 detects pressure in fluid and sensor 2-4 measure the displacement of the points on the shell. The reference positions of sensors 2-4 are measured from the center of the undeformed cylinder, but still account for ovality.

This diagram features three unique fluid domains: two gaseous domains and one liquid domain. The liquid domain is the ambient fluid, or water surrounding the cylindrical shell. The other two gaseous domains include the explosion byproduct in the bubble on the top portion of the figure and the air located inside the empty cylindrical shell on the bottom part of the figure.

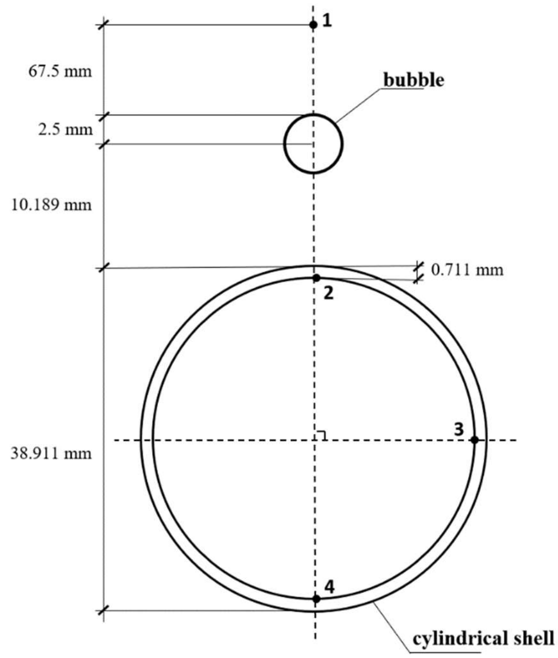


**FIGURE 1:** Experimental model diagram and dimensions.

Because there is a large variation in pressure due to the shock waves created from the explosion, the medium's behavior is modeled with the Navier-Stokes equations, *Equation (1)* and the fluid is treated as compressible.

$$\frac{\partial W(x,t)}{\partial \mathrm{t}} + \nabla \cdot F(W) = \nabla \cdot G(W, \nabla W) \tag{1}$$

The terms *W, F,* and *G* are described as follows.

$$W = \begin{bmatrix} \rho \\ \rho \mathrm{V} \\ \rho \mathrm{e}_t \end{bmatrix}, F = \begin{bmatrix} \rho \mathrm{V}^T \\ \rho \mathrm{V} \otimes V + \mathrm{p}\mathbf{I} \\ (\rho \mathrm{e}_t + p) V^T \end{bmatrix}, G = \begin{bmatrix} 0 \\ \boldsymbol{\tau} \\ V^T \boldsymbol{\tau} - Q^T \end{bmatrix} \tag{2}$$

In these equations, capitalized letters correspond to vector quantities, lowercase letters correspond scalar quantities, and bolded letters correspond to second-order tensors. $\rho$ is the fluid's density, $\mathrm{V}$ is the velocity, $\mathrm{e}_t$ is the total energy per unit mass in the system, $p$ is the pressure, $\boldsymbol{\tau}$ is the viscous stress tensor, $\mathbf{I}$ is the 3×3 identity matrix, the superscript $T$ denotes the transpose of the given vector, and $Q$ is the heat flux.

It should be noted that body forces such as gravity are neglected in *Equations (1) and (2)*, and sources of heat have been neglected as well. To simplify the calculations in the solver, viscosity and heat diffusion are also ignored, which reduces *Equation (1)* to the Euler equations, *Equation (3).* This simplified equation models inviscid flow and allows the solver to utilize fewer resources.

$$\frac{\partial W(x,t)}{\partial t} + \nabla \cdot F(W) = 0 \quad (3)$$

The Tait equation of state (EOS) is utilized for the liquid water surrounding both the bubble and cylindrical shell. This equation establishes a relationship between the pressure of the fluid and the density of the fluid, allowing for the liquid water to be treated as compressible. This is necessary due to the extreme loading conditions and large pressure variations produced by the shock waves. The air inside the cylindrical shell follows the ideal gas law.

To simplify modelling farther, the explosion from the detonation of a charge is modeled as a small, high-pressure air bubble following the ideal gas law. To track the progression of the bubble, the level-set equation, *Equation (4)*, is solved where $\phi$ denotes a function that tracks the interface between exactly two constituents. $v$ is the velocity vector of the fluid.

$$\frac{\partial \phi}{\partial t} + v \cdot \nabla \phi = 0 \quad (4)$$

The simulation in this paper utilized the FIVER method (Finite Volume method with Exact multi-material Riemann solvers) to resolve the collapse of the cylindrical shell. This solver is able to account for the interactions between the fluid domain and the structural body and will deform the body as is appropriate. The fluid mesh is entirely rigid throughout the simulation and does not deform. Instead, an imbedded boundary method tracks the wetted surface of the submerged cylinder and interfaces the interactions between the two meshes, overlaying the continuously deforming cylindrical mesh over the fixed fluid mesh. This method allows for large deformations of the structural mesh and does not require the large computational power another solver might require to deform the fluid mesh along with the structural mesh. This finite volume mesh is unstructured, node-centered, and is non-interface-conforming.

An augmented fluid domain is used, which includes all the subdomains as well as the fluid domain inside of the cylinder and the fluid domain inside of the bubble. The Euler equations are integrated across $C_i$, an arbitrary control volume, to produce *Equation (5)*.

$$\frac{\partial W_i}{\partial t} + \frac{1}{||C_i||} \sum_{j \in N(i)} \int_{\partial C_{\text{ij}}} F(W) \cdot \boldsymbol{n}_{\text{ij}} \, dS = 0 \quad (5)$$

In *Equation (5)* $W_i$ is the average fluid state vector $W$ in the total control volume $C_i$. $N(i)$ is the vector of nodes that are connected to the i$^{\text{th}}$ node by their edge. $\partial C_{\text{ij}} = \partial C_i \cap C_j$ is the boundary faces for the two control volumes. $\boldsymbol{n}_{\text{ij}}$ is the unit tensor that faces normal to the boundary faces $\partial C_{\text{ij}}$. From this information, the flux can be calculated in unique ways which are dependent on the locations of nodes i and j. These unique ways are dependent on the subdomain that the node belongs to.

*Equation 6* describes a structure undergoing finite deformation, and it is modeled in the Lagrangian setting.

$$\rho_s \frac{\partial^2 u_j}{\partial t^2} = \frac{\partial}{\partial x_i}(\tau_{\text{ij}} + \tau_{\text{im}} \frac{\partial u_j}{\partial x_m}) + b_j \quad (6)$$

In *Equation (6)*, the subscripts *i, j,* and *m* are used to denote values between 1 and 3 and designate a direction in the cartesian $(x, y, z)$ coordinate system. The density of the undeformed structure is denoted by $\rho_s$, the second Piola-Kirchoff stress is denoted by $\tau$, the nodal displacement vector is denoted by $u$, and *b* denotes the body force vector. The body force *b* is 0 in this paper as external forces directly acting on any internal portion of the cylindrical shell are neglected.

Geometric and material nonlinearities of aluminum is properly described by a constitutive model based on Green's second-order strain tensor and second Piola-Kirchhoff stress tensor. Plasticity of aluminum follows the J2 yield criterion with isotropic hardening.

Additional details of the FIVER framework can be found in references [24-32]. Over the past decades, FIVER has been applied to several fluid-structure interaction problems including underwater hydrostatic implosion [33-35], pipeline explosion [36,37], shock wave lithotripsy [38-41], bio-mimetic propulsors [42], and supersonic parachute deployment [43]. Several verification and validation studies have also been conducted. For example, Farhat *et al*. [33] showed that for an underwater implosion problem the structural dynamics and fluid pressure predicted by FIVER match closely with the experimental data. Main *et al*. [31] showed that for another implosion experiment, FIVER is able to accurately capture the shock wave resulting from bubble collapse. More recently, Cao et al. [41] validated FIVER and the level set method for the collapse of a bubble in free field and near different solid materials.

## 3. RESULTS AND DISCUSSION

This numerical experiment investigates a thin cylindrical aluminum shell with material properties detailed in *Table 1* and geometric/finite element properties detailed in *Table 2*. This model assumes the cylindrical shell has infinite length, however for modelling purposes an axial thickness must be prescribed. In this experiment, the finite element mesh is only one element deep and has a thickness of 0.4 mm. The material properties correspond with Aluminum 6061-T6. The ovality of the cylinder was established based off of a sinusoidal function that would modify a perfect cylinder to have two modes of imperfection. These two modes of imperfection will work to push the structure to collapse in mode 2. Although difficult to see in *Figure 1*, the direction of the ovality occurs so that the left- and right-hand sides of the structure are slightly closer to each other, and the bottom and top sides of the structure are slightly farther away.

**Table 1: Cylindrical Shell Material Properties**

| Young's Modulus | Poisson's Ratio | Density | Yield Stress | Tangent Modulus |
|---|---|---|---|---|
| 70.8 GPa | 0.33 | 2780 kg/$m^3$ | 30.4 GPa | 66.74 GPa |

| Table 2: Cylindrical Shell Geometric / Element Properties | | | | |
|---|---|---|---|---|
| Outer Diameter | Thickness | Ovality | # Layers | # elements per layer |
| 38.911 mm | 0.711 mm | 0.1% | 5 | 400 |

*Table 3* denotes information regarding both the bubble's geometry and the fluid medium's properties. Besides, the initial pressure of the air inside the shell is 0.1 MPa with an initial density of 1.225 kg/m$^3$. It should be noted that the bubble distance is the distance from the center of the bubble to the outer wall of the cylinder. These dimensions can be seen in *Figure 1*.

| Table 3: Bubble/Fluid Characteristics and Geometry | | | | |
|---|---|---|---|---|
| Bubble Distance | Bubble Radius | Bubble Pressure | Fluid Speed of Sound | Hydrostatic Pressure |
| 10.189 mm | 2.5 mm | 12.5 MPa | 1,513.4 m/s | 1.0 MPa |

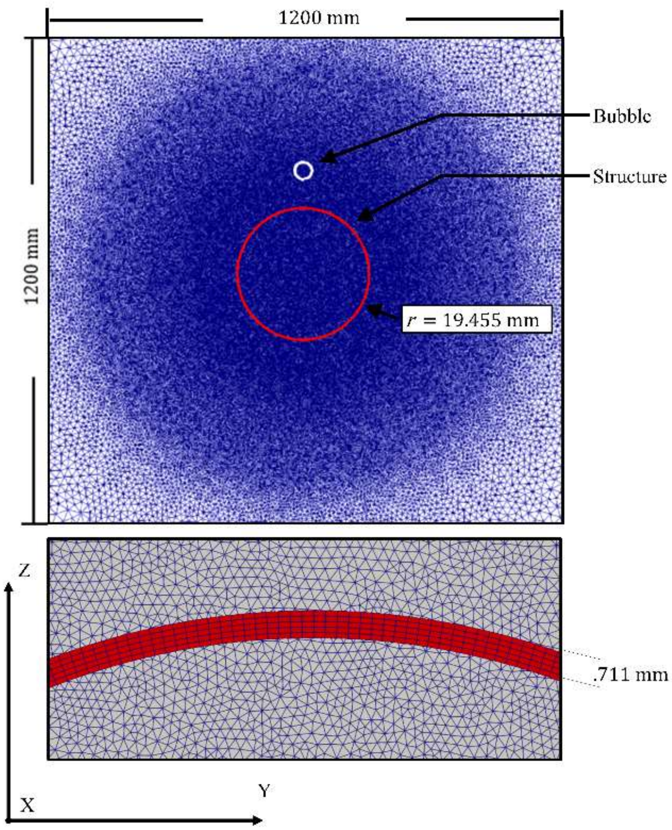


**Figure 2:** A visual overlay of the non-conforming fluid mesh and the thin cylindrical shell structural mesh. Note that the overall fluid mesh dimension (*1200 mm*) is not to scale as the entire fluid mesh was too large to be encapsulated in the image.

*Figure 2* shows the fluid mesh (blue) and structural mesh (red). The inside of the cylinder is meshed to model the air there. To increase the accuracy of the results and the stability of the simulation, the size of one element of the fluid mesh is approximately the same as the size of a structural mesh element at the interface between the two. The centermost portion of the meshes has the highest element density, as most of the interactions occur in that region. As seen in the top subfigure, the mesh resolution decreases as the distance from the structure increases.

*Table 4* presents three different computation grids for a mesh refinement study. Solid element density is the number of elements in circumferential and radial directions in the cylindrical shell, e.g., Grid 2 has 5 brick elements through the thickness and 400 elements in one revolution of the cylinder. Finest fluid cell size is the grid size at the interface of fluid mediums and the aluminum cylinder.

| Table 4: Computation Grids | | | |
|---|---|---|---|
| | Solid Element Density | # Fluid Cells | Finest Fluid Cell Size (mm) |
| Grid 1 | 200 × 3 | 0.607×10$^6$ | 0.6 |
| Grid 2 | 400 × 5 | 0.689×10$^6$ | 0.3 |
| Grid 3 | 600 × 5 | 4.537×10$^6$ | 0.2 |

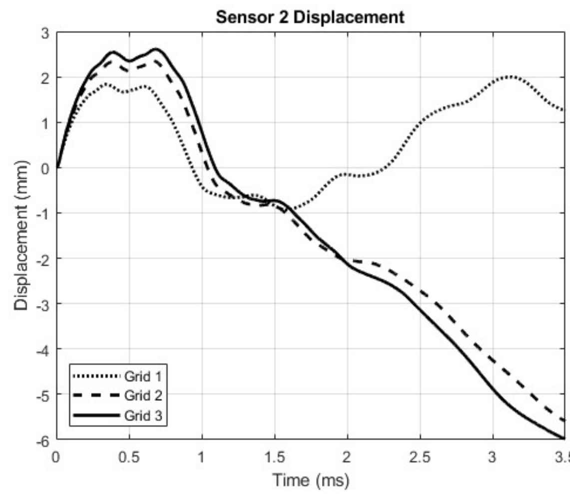


**Figure 3:** Displacement of sensor 2 for three different element densities

*Figure 3* shows the displacement at sensor 2 (the one directly facing the bubble in *Figure 1*) for the three grids listed in Table 4. Results from Grid 2 and the much finer Grid 3 agree reasonably well. The maximum difference between the two curves is about 10% occurring near the end of the curves. Because of the significantly less computation resource required by Grid 2, the following results in this paper are from the simulation on Grid 2.

*Figure 4* features a time-history of the collapse of the submerged cylinder paired with the oscillation number of the bubble. Each image in the figure corresponds with one half-cycle of bubble expansion or compression, where lighter shades are earlier time steps and darker shades are later time steps. In each cycle, the left figure showcases the expansion of the bubble, and the right figure showcases the collapse of the bubble. The bubble is located towards the top of the figure, and the cylindrical shell is the larger body towards the bottom of the figure. As observed in Figure 4, the cylindrical shell collapses in a counter-intuitive mode/orientation in which the point facing the explosion moves toward the explosive bubble. Ikeda [44] observed similar collapse behavior on Aluminum shells with similar geometry under similar experiment setup.

Cycle 1 is the initial formation of the bubble, where the expansion of the bubble lasts 0.566 ms and the compression of the bubble lasts 0.834 ms. During the first half of the cycle, the bubble maintains an almost purely circular shape as it expands, and the structure begins to ovalize with the longer axis corresponding to the y-axis (denoted at the bottom of *Figure 3*). During the second half of cycle 1, the bubble compresses again and begins to lose its circular shape. A dent is formed along its bottom side and protrudes towards the center of the bubble. During this process, the structure does not continue to be compressed in z-direction and instead begins to be compressed in the y-direction at ~0.4 ms, near the end of the first half cycle. The top of the structure appears to deform in the same direction the dent is forming inside the bubble and undergoes a larger magnitude of deformation than in the first half of the cycle. Before ~0.4 ms, the structure is deformed against the initial ovality, and after that the structure is deformed with the initial ovality. This deformed configuration could be described as an exaggeration of the initially prescribed ovality.

The first half of cycle 2 lasts 0.7 ms, and the second half of cycle 2 lasts 0.6 ms. During both the expansion and the collapse of this cycle, the structure continues to collapse symmetrically about the z-axis. The dent in the bottom side of the bubble continues to perturb through it and increases in magnitude.

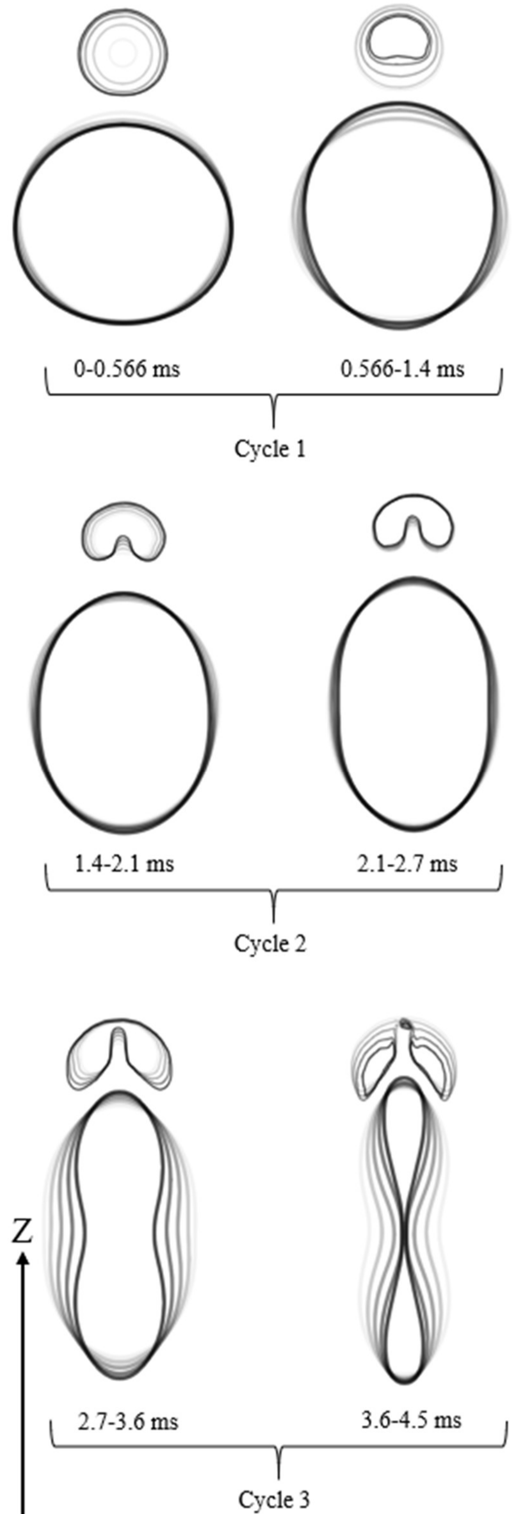


**Figure 4:** Collapse cycle of the bubble paired with motion of the cylindrical shell. Each image in the figure corresponds with one half-cycle of bubble expansion or compression, where lighter shades are earlier time steps and darker shades are later time steps.

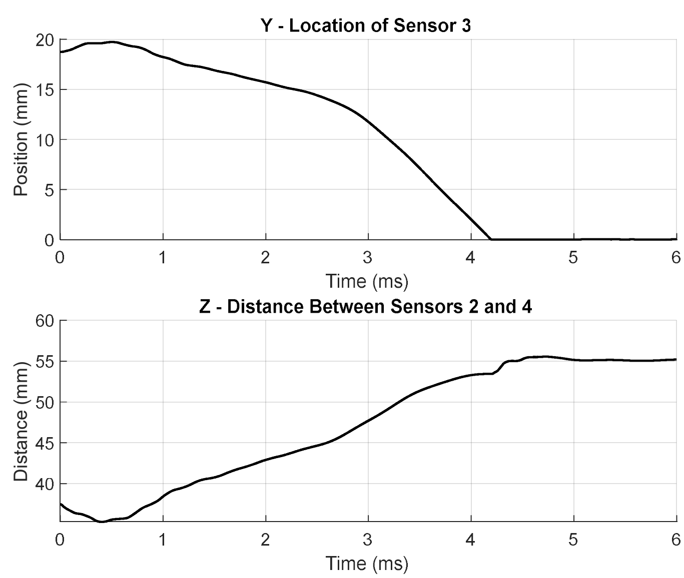


**Figure 5:** The y-directional location of sensor 3 and the absolute z-directional distance between sensors 2 and 4.

The first half of cycle 3 last 0.9 ms and the second half of cycle 3 also lasts 0.9 ms. It is during this cycle that the bubble splits into two smaller bubbles and the structure collapses. During the expansion, the dent in the bubble almost perturbs through the top of it and the structure undergoes the largest magnitude of deformation. During the second half of the cycle,

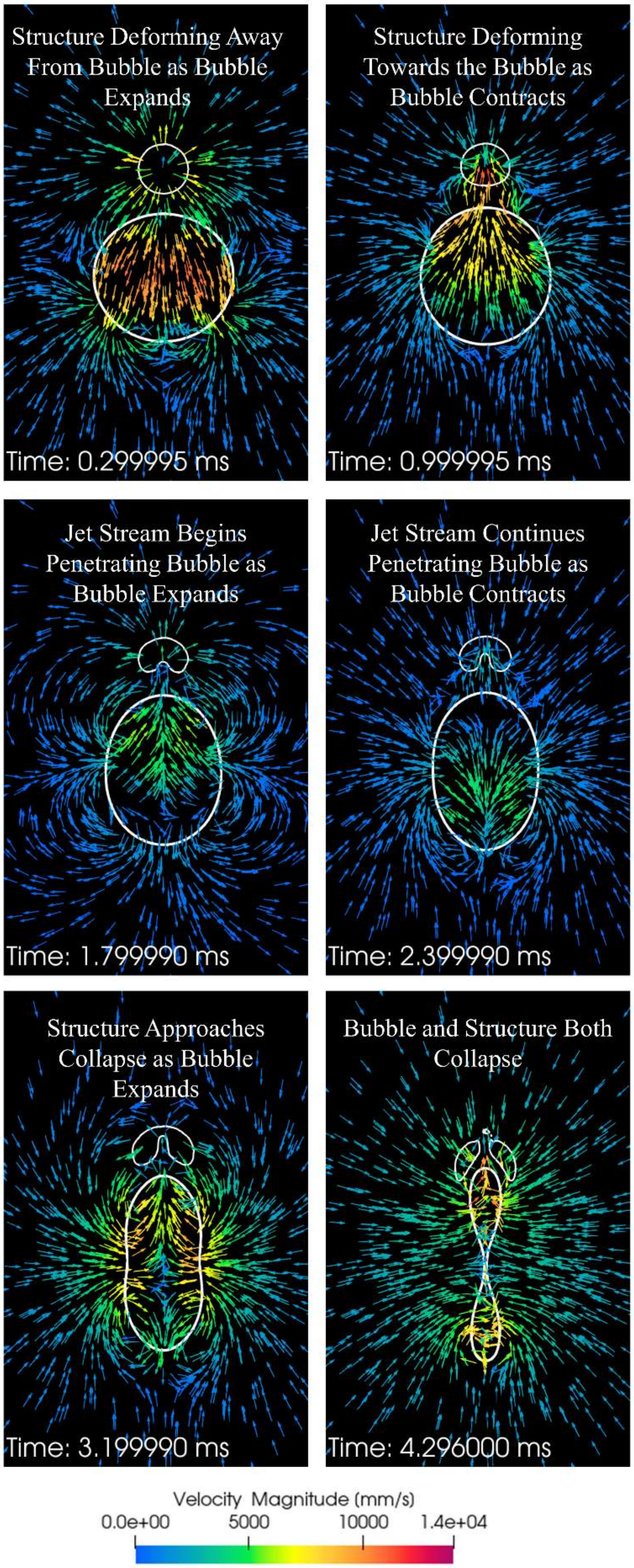


**Figure 6:** Velocity field of the fluid medium for each half-cycle oscillation of the bubble.

the bubble finally splits through the middle and breaks into two smaller primary bubbles, with a third smallest bubble located above and in-between the two. During this stage, the structure also reaches its final collapse where the left and right sides meet.

*Figure 5* shows the displacement at each of the sensors shown in *Figure 1*. The top figure features the y-directional position of the sensor 90 degrees clockwise around the structure from the bubble (origin is at the centroid of cylinder), and the bottom figure features the absolute z-directional distance between sensors 2 and 4. These figures give a better insight towards the motions of the cylindrical shell during collapse.

During the most time of the first bubble half-cycle since explosion, sensor 3 travels farther away from the center of the cylindrical shell, while sensors 2 and 4 move closer together. However, near the end of the first bubble half-cycle, sensor 3 begins approaching the centroid of the shell, while sensors 2 and 4 grow farther apart. The cylindrical shell finally collapses at 4.192 ms where sensor 3 touches the opposite side of the wall. There is a brief period where the collided sections of the structure flatten in the z-direction, but this motion quickly stops, leaving two bulges at either end of the cylinder. After the structure has collapsed at 4.192 ms, sensors 2, 3, and 4 remain primarily stationary and only move a few fractions of a millimeter as residual forces interact with the structure.

*Figures 6* and *7* show the velocity field and the pressure field of the fluid medium, respectively. The first image in *Figure 7* shows the initial state of the system, and the remaining images correspond with an instance of time approximately midway through each half-oscillation of the bubble. Although the maximum value of the pressure scale in *Figure 7* is 2.0 MPa, the maximum pressure inside the bubble is 12.5 MPa. This scale range was chosen as most of the interesting behavior occurs in this range, and the initial pressure inside of the bubble dissipates quickly. In *Figure 7*, the structure is colored by the effective plastic strain. As the shell collapses, plastic deformation first occurs at the top and bottom portion of the shell and then at the left and right. *Figure 8* includes a pair of plots that include (in descending order) the pressure detected at sensor 1 from the shock wave and bubble oscillation, as well as the bubble's average radius.

During the first half-cycle of the bubble's oscillation, the initial shock wave from the bubble's expansion hits the structure with a strength of 3.276 MPa detected at sensor 1. A lower pressure region can be seen enveloping the bubble and the entire cylindrical shell, which has pressures much lower than the hydrostatic pressure of 1.0 MPa. Throughout this period, water flows away from the bubble in all directions.

When the bubble begins to collapse in the second half-cycle of its oscillation, the outward flow from the bubble begins to turn inward and the pressure above the shell reaches a minimum. The cylinder begins to collapse about the z-axis instead of the y-axis. Although the bubble has flows coming from all directions, the flow directly between the structure and the bubble is the largest in magnitude, and a jet can be seen forming between them in the second frame of *Figure 6*.

At the beginning of the second bubble cycle, the pressure around the bubble and cylindrical shell is at a local maximum and begins to decrease (at 1.4 ms in *Figure 8*). Due to this, the bubble begins to expand again, and the flow diverges from the bubble (shown in the third frame of *Figure 6*). Despite this divergence, there is still a mild jet stream between the shell and the bubble that causes for the dent in the bubble to increase. This corresponds with the top point of the shell continuing to travel upwards while the bottom point moves downwards. During the second portion of the second cycle (the fourth frame of *Figure 6*), the bubble shrinks again, and the jet stream becomes slightly stronger. The structure continues to deform in the same motion as previously discussed.

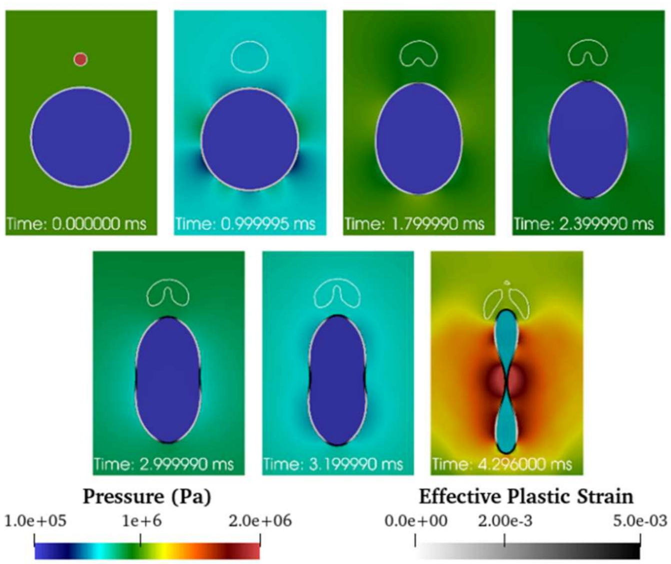


**Figure 7:** Pressure field time-history starting with the initial conditions, and then showing one instance of time from each half-oscillation of the bubble.

When the bubble begins to expand again at the beginning of cycle 3, the fifth frame of *Figure 6* shows the flow diverging from the bubble in all directions except for the jet stream between the structure, which continues to flow towards the bubble. This flow pattern continues to facilitate the upward motion of the shell's top point and the downward motion of the shell's bottom point. At ~3.3 ms, the water around the upper section of the bubble reverses direction and begins to flow downwards, towards the bubble. The water around the lower-left and lower-right portions of the bubble continues to flow away, but at a higher velocity. This flow is accompanied by growth in the left and right lobes of the bubble, causing for them to become more pronounced.

Once the bubble undergoes the second part of its third cycle, the jet in the last frame of *Figure 6* penetrates through to the other side and the two lobes of the bubble separate at ~3.8 ms. The structure continues to collapse until ~4.2 ms, when the two edges in the middle meet. When these edges meet, a shock wave is emitted from the contact point as the water around it was suddenly stopped.

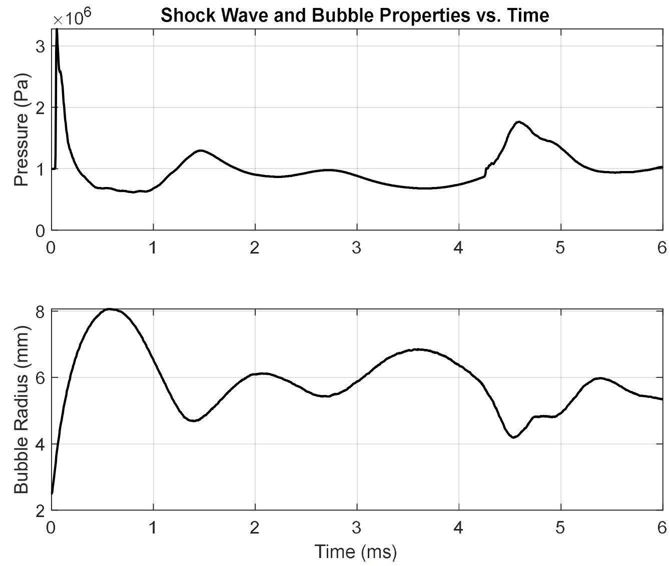


**Figure 8:** Time-history of overpressure delivered from the shock wave and the average bubble radius.

These findings can be all be visually seen by comparing results from *Figures 4-8*, which encapsulate the full behavior of collapse. *Figure 4* is broken down into six sub-images, which each shows the structure's time-history about a half-cycle of the bubble's oscillation. The top 2 images show (in tandem with *Figure 5*) that the cylindrical shell begins to be compressed in the z-direction and then resists the initial deformation. After this first half-cycle, *Figure 5* shows that the structure continues to separate between sensors 2 and 4 until the entire body collapses. *Figure 6* details the fluid dynamics surrounding the structure, which illustrates how a jet stream was formed to penetrate the bubble. *Figure 8* can then be viewed in tandem with *Figure 6* to visualize the bubble's change in average radius, and the pressure pulses' history. *Figure 7* then serves as a broad overview of how the pressure field fluctuates around the shell at various instances of time, and farther illustrates influences on the collapse of the structure.

## 4. CONCLUSION

In this paper, we applied a fluid-structure coupled computational framework to model and simulate the interaction between an underwater cylindrical shell and an explosive bubble generated by a near-field underwater explosion. The motion of both the explosive bubble and cylindrical shell, as well as the dynamics of flow field were analyzed. Under certain situation like the one presented in this paper, the cylindrical shell collapses in a counter-intuitive mode/orientation in which the point facing the explosion moves toward the explosive bubble. The moving direction of this collapse mode/orientation is consistent with the liquid jet that diverges from the structure and penetrates through the bubble during the bubble pulsations. Both the collapse mode and the liquid jet occur under the effects of the interaction between the explosive bubble, the cylindrical shell, and the surrounding liquid. Additional studies are being performed to understand the underlying mechanisms.

## ACKNOWLEDGEMENTS

The authors gratefully acknowledge the support of the Office of Naval Research (ONR) under Awards N00014-19-1-2102, and the support of the National Science Foundation (NSF) under Awards CBET-1751487.

## REFERENCES

[1] Michael M Swisdak. Explosion Effects and Properties. Part II. Explosion Effects in Water. Technical Report NSWC/WOL TR 76-116, Naval Surface Weapons Center, White Oak, Silver Spring, MD 20910, USA, 1978.

[2] Young S. Shin. Ship Shock Modeling and Simulation for Far-Field Underwater Explosion. *Computers and Structures*, 82(23-26):2211–2219, 2004.

[3] L. Loureiro Silva, and T. A. Netto. On the Dynamic Collapse of Cylindrical Shells Under Hydrostatic and Impulsive Pressure Loadings: Experimental and Numerical Analysis. In *ASME 2011 30th International Conference on Ocean, Offshore and Arctic Engineering,* ASME Paper No. OMAE2011-49361, pp. 299-306, 2011.

[4] Jianyu Wu, Ji Chong, Yuan Long, You Zhou, Yang Yu, and Jianfeng Liu. Experimental Study on the Deformation and Damage of Cylindrical Shell-Water-Cylindrical Shell Structures Subjected to Underwater Explosion. *Thin-Walled Structures*, 127:654–65, 2018.

[5] E. Klaseboer, B.C. Khoo, and K.C. Hung. Dynamics of an Oscillating Bubble near a Floating Structure. *Journal of Fluids and Structures*, 21(4):395–412, 2005.

[6] Shuai Li, A-Man Zhang, Rui Han, and Qingwei Ma. 3D Full Coupling Model for Strong Interaction between a Pulsating Bubble and a Movable Sphere. *Journal of Computational Physics*, 392:713–731, 2019.

[7] A.M. Zhang, X.L. Yao, and J. Li. The Interaction of an Underwater Explosion Bubble and an Elastic–Plastic Structure. *Applied Ocean Research*, 30(3):159–171, 2008.

[8] Jian Li, and Ji-Li Rong. Experimental and Numerical Investigation of the Dynamic Response of Structures Subjected to Underwater Explosion. *European Journal of Mechanics - B/Fluids*, 32:59–69, 2012.

[9] Jia-Xia Wang, Zhi Zong, Kun Liu, and Jie Cui. Simulations of the Dynamics and Interaction between a Floating Structure and a near-Field Explosion Bubble. *Applied Ocean Research*, 78:50–60, 2018.

[10] Lorenzo Maria Bartolini, Lorenzo Marchionni, Caterina Molinari, and Antonio Parrella. Effects of Underwater Explosion on Pipeline Integrity. In *ASME 2015 34th International Conference on Ocean, Offshore and Arctic Engineering,* ASME Paper No. OMAE2015-41092, V05AT04A004, 2015.

[11] John M. Brett, and George Yiannakopolous. A Study of Explosive Effects in Close Proximity to a Submerged Cylinder. *International Journal of Impact Engineering*, 35(4):206–25, 2008.

[12] Ching-Yu Hsu, Cho-Chung Liang, Anh-Tu Nguyen, and Tso-Liang Teng. A Numerical Study on the Underwater Explosion Bubble Pulsation and the Collapse Process. *Ocean Engineering*, 81:29–38, 2014.

[13] Nu Zhang, Zhi Zong, and Wenpeng Zhang. Dynamic Response of a Surface Ship Structure Subjected to an Underwater Explosion Bubble. *Marine Structures*, 35:26–44, 2014.

[14] A-Man Zhang, Shi-Ping Wang, Chao Huang, and Bin Wang. Influences of Initial and Boundary Conditions on Underwater Explosion Bubble Dynamics. *European Journal of Mechanics - B/Fluids*, 42:69–91, 2013.

[15] Stelios Kyriakides and Edmundo Corona. Mechanics of Offshore Pipelines, Volume 1: Buckling and Collapse. Elsevier Science, 2007.

[16] C. M. Ikeda, J. Wilkerling, and J. H. Duncan. The Implosion of Cylindrical Shell Structures in a High-Pressure Water Environment. *Proceedings of the Royal Society A: Mathematical, Physical and Engineering Sciences*, 469(2160):20130443, 2013.

[17] T.-D. Park and S. Kyriakides. On the Collapse of Dented Cylinders under External Pressure. *International Journal of Mechanical Sciences*, 38(5): 557–578, 1996.

[18] J.Y. Dyau and S. Kyriakides. On the Localization of Collapse in Cylindrical Shells under External Pressure. *International Journal of Solids and Structures*, 30(4):463–482, 1993.

[19] Wendell B. Stephens, James H. Starnes, and B. O. Almroth. Collapse of Long Cylindrical Shells under Combined Bending and Pressure Loads. *AIAA Journal*, 13(1):20–25, 1975.

[20] Muntaseer Kainat, J. J. Roger Cheng, Michael Martens, and Samer Adeeb. Measurement and Characterization of the Initial Geometric Imperfections in High Strength U-ing, O-ing and Expanding Manufactured Steel Pipes. *Journal of Pressure Vessel Technology*, 138(2):021201, 2015.

[21] Muntaseer Sarwar-E-Kainat. Initial Imperfections of High Strength UOE Manufactured Steel Pipes and Their Effects on Pipe Buckling. Ph.D. dissertation, University of Alberta, Canada, 2014.

[22] Konstantinos Antoniou, Giannoula Chatzopoulou, Spyros A. Karamanos, Athanasios Tazedakis, Christos Palagas, and Efthimios Dourdounis. Numerical Simulation of JCO-E Pipe Manufacturing Process and Its Effect on the External Pressure Capacity of the Pipe1. *Journal of Offshore Mechanics and Arctic Engineering*, 141(1):011704, 2019.

[23] Jian-Xing Yu, Meng-Xue Han, Jing-Hui Duan, Yang Yu, and Zhen-Zhou Sun. A Modified Numerical Calculation Method of Collapse Pressure for Thick-Walled Offshore Pipelines. *Applied Ocean Research*, 91:101884, 2019.

[24] Charbel Farhat, Jean-Frédéric Gerbeau, and Arthur Rallu. FIVER: A Finite Volume Method Based on Exact Two-Phase Riemann Problems and Sparse Grids for Multi-

Material Flows with Large Density Jumps. *Journal of Computational Physics*, 231(19):6360–6379, 2012.
[25] Alex Main, Xianyi Zeng, Philip Avery, and Charbel Farhat. An Enhanced FIVER Method for Multi-Material Flow Problems with Second-Order Convergence Rate. *Journal of Computational Physics*, 329:141–172, 2017.
[26] Kevin Wang, Arthur Rallu, J-F Gerbeau, and Charbel Farhat. Algorithms for Interface Treatment and Load Computation in Embedded Boundary Methods for Fluid and Fluid–structure Interaction Problems. *International Journal for Numerical Methods in Fluids*, 67(9):1175–1206, 2011.
[27] Charbel Farhat, Arthur Rallu, and Sriram Shankaran. A Higher-order Generalized Ghost Fluid Method for the Poor for the Three-dimensional Two-phase Flow Computation of Underwater Implosions. *Journal of Computational Physics*, 227(16):7674–7700, 2008.
[28] C Farhat, A Rallu, K Wang, and T Belytschko. Robust and Provably Second-order Explicit–explicit and Implicit–explicit Staggered Time-integrators for Highly Non-linear Compressible Fluid–structure Interaction Problems. *International Journal for Numerical Methods in Engineering*, 84(1):73–107, 2010.
[29] Kevin Wang, J Gretarsson, A Main, and C Farhat. Computational Algorithms for Tracking Dynamic Fluid–structure Interfaces in Embedded Boundary Methods. *International Journal for Numerical Methods in Fluids*, 70(4):515–535, 2012.
[30] Kevin Wang, Jon Gretarsson, Alex Main, and Charbel Farhat. Computational Algorithms for Tracking Dynamic Fluid-structure Interfaces in Embedded/immersed Boundary Methods. In *20th AIAA Computational Fluid Dynamics Conference*, page 3385, 2011.
[31] Alex Main and Charbel Farhat. A Second-order Time Accurate Implicit Finite Volume Method with Exact Two-phase Riemann Problems for Compressible Multi-phase Fluid and Fluid–structure Problems. *Journal of Computational Physics*, 258:613–633, 2014.
[32] Daniel Z Huang, Dante De Santis, and Charbel Farhat. A Family of Position-and Orientation-independent Embedded Boundary Methods for Viscous Flow and Fluid–structure Interaction Problems. *Journal of Computational Physics*, 365:74–104, 2018.
[33] C Farhat, KG Wang, A Main, Stelios Kyriakides, L-H Lee, Krishnaswa Ravi-Chandar, and T Belytschko. Dynamic Implosion of Underwater Cylindrical Shells: Experiments and Computations. *International Journal of Solids and Structures*, 50(19):2943–2961, 2013.
[34] Kevin G Wang, Patrick Lea, Alex Main, Owen McGarity, and Charbel Farhat. Predictive Simulation of Underwater Implosion: Coupling Multi-material Compressible Fluids with Cracking Structures. In *ASME 2014 33rd International Conference on Ocean, Offshore and Arctic Engineering*, ASME Paper No. OMAE2014-23341, V08AT06A028, 2020.
[35] Wentao Ma, Xuning Zhao, and Kevin Wang. A Fluid-Structure Coupled Computational Model for the Certification of Shock-Resistant Elastomer Coatings. In *ASME 2020 39th International Conference on Ocean, Offshore and Arctic Engineering*, ASME Paper No. OMAE2020-18501, V02AT02A024, 2020.
[36] Kevin G Wang, Patrick Lea, and Charbel Farhat. A Computational Framework for the Simulation of High-Speed Multi-Material Fluid-Structure Interaction Problems with Dynamic Fracture. *International Journal for Numerical Methods in Engineering,* 104(7): 585–623, 2015.
[37] Patrick D Lea, Charbel Farhat, and Kevin G Wang. A Fluid-structure Coupled Computational Framework for Fluid Induced Failure and Fracture. In *ASME 2015 34th International Conference on Ocean, Offshore and Arctic Engineering*. American Society of Mechanical Engineers Digital Collection, 2015.
[38] Shunxiang Cao, Ying Zhang, Defei Liao, Pei Zhong, and Kevin G Wang. Assessing the Effect of Lithotripter Focal Width on the Fracture Potential of Stones in Shockwave Lithotripsy. *The Journal of the Acoustical Society of America*, 141(5):3718–3718, 2017.
[39] Kevin G Wang. Multiphase Fluid-solid Coupled Analysis of Shock-bubble-stone Interaction in Shockwave Lithotripsy. *International Journal for Numerical Methods in Biomedical Engineering*, 33(10):e2855, 2017.
[40] Shunxiang Cao, Ying Zhang, Defei Liao, Pei Zhong, and Kevin G Wang. Shock-induced Damage and Dynamic Fracture in Cylindrical Bodies Submerged in Liquid. *International Journal of Solids and Structures*, 169:55–71, 2019.
[41] Shunxiang Cao, Guangyao Wang, Olivier Coutier-Delgosha, and Kevin Wang. Shock-induced Bubble Collapse near Solid Materials: Effect of Acoustic Impedance. *Journal of Fluid Mechanics*, 907:A17, 2021.
[42] Howard Chung, Shunxiang Cao, Michael Philen, Philip S Beran, and Kevin G Wang. CFD-CSD Coupled Analysis of Underwater Propulsion Using a Biomimetic Fin-and-joint System. *Computers & Fluids*, 172:54–66, 2018.
[43] Daniel Z Huang, Philip Avery, Charbel Farhat, Jason Rabinovitch, Armen Derkevorkian, and Lee D Peterson. Modeling, Simulation and Validation of Supersonic Parachute Inflation Dynamics during Mars Landing. In *AIAA Scitech 2020 Forum*, page 0313, 2020.
[44] Christine M. Ikeda. Fluid Structure Interactions: Implosions of Shell Structures and Wave Impact on a Flat Plate. Ph.D. dissertation, University of Maryland, College Park, 2012.